Electronic Supplementary Information for

Self-driven dual hydrogen production system based on bifunctional single-atomic Rh catalyst

Xianyun Peng[1,2], Yuying Mi[2], Xijun Liu[1,2]*, Jiaqiang Sun[3], Yuan Qiu[2], Shusheng Zhang[4], Xiaoxing Ke[5], Xinzhong Wang[1]*, and Jun Luo[2]*

[1] Information Technology Research Institute, Shenzhen Institute of Information Technology, Shenzhen 518172, China.

[2] School of Materials Science and Engineering, Tianjin Key Lab of Photoelectric Materials & Devices, Tianjin University of Technology, Tianjin 300384, China.

[3] State Key Laboratory of Coal Conversion, Institute of Coal Chemistry, Chinese Academy of Sciences, Taiyuan 030001, China.

[4] College of Chemistry, Zhengzhou University, Zhengzhou 450000, China.

[5] Beijing Key Laboratory of Microstructure and Properties of Solids, Faculty of Materials and Manufacturing, Beijing University of Technology, Beijing 100124, China.

* e-mail: xjliu@tjut.edu.cn (X.J.L.), wangxz@sziit.com.cn (X.Z.W.), jluo@email.tjut.edu.cn (J.L.)

Experimental Section

Synthesis of Rh-SA/$Ti_3C_2O_x$

To synthesize the Rh-SA/$Ti_3C_2O_x$, 1 g of lithium fluoride (LiF) powder was added to 10 mL of 9 M HCl solution. The mixture was stirred for 5 min with a magnetic Teflon stir bar to dissolve the salt. 1 g of Ti_3AlC_2 powder was slowly and carefully added to the above mixture over 0.5 h to avoid initial overheating of the solution as a result of the exothermic nature of the reactions. Subsequently, 1 mL of 1 mg mL^{-1} freshly prepared rhodium chloride hydrate ($RhCl_3 \cdot xH_2O$) solution was added to the solution. The reaction mixture was held at 35 °C in a water bath for 24 h, after which the mixture was washed with deionized water several times by centrifugation until the pH of the supernatant reached approximately 6. The collected sediments from the last centrifugation were dispersed in 50 mL deionized water. The mixture was vigorously ultrasonicated for 1 h under a flowing Ar atmosphere in an ice bath to minimize oxidation. After that, the solution was centrifuged at 3500 rpm for 1 h and the dark-green supernatant was collected. Thereafter, the colloidal suspension (50 mL) was mixed with 50 ml KOH solutions (10 wt%) in the presence of Ar atmosphere for 4 h at room temperature. Then, the alkalization mixture was obtained by washing with deionized water by centrifugation and freeze-drying. Finally, the Rh-SA/$Ti_3C_2O_x$ was obtained by annealing the freeze-dried product at 350 °C for 5 h at a heating rate of 5°C min^{-1} in a tube furnace under an Ar atmosphere (50 sccm).

Synthesis of $Ti_3C_2O_x$

The $Ti_3C_2O_x$ was prepared using a similar procedure to the one described above for Rh-SA/$Ti_3C_2O_x$, except that no Rh precursor was added.

Synthesis of Rh-NP/$Ti_3C_2O_x$

For the synthesis of Rh-NP/$Ti_3C_2O_x$, 50 mg of $Ti_3C_2O_x$ was firstly dissolved in 50 mL of water in a round-bottom flask, then sonicated for 30 min to obtain a uniform dispersion. Then, 5 mL of 1 mg mL^{-1} $RhCl_3 \cdot xH_2O$ aqueous solution was added into the above $Ti_3C_2O_x$ solution gently, with electromagnetic stirring for 30 min. Then, 50 mg of sodium borohydride ($NaBH_4$) dissolved in 1 ml of 2 M NaOH solution was quickly added

into the above resultant mixture under vigorous stirring 2 h and then ultrasonic treatment 2 h at 0 °C using an ice bath under a flowing Ar atmosphere. Subsequently, the resulting solution was washed with deionized water by centrifugation. Finally, the Rh-NP/$Ti_3C_2O_x$ composite was obtained by freeze-drying.

Materials Characterization

X-ray diffraction (XRD) patterns of the samples were obtained by a Rigaku D/max 2500 X-ray diffractometer with a Cu Kα radiation source (λ = 0.154598 nm). The morphology and structure of the samples were characterized by using transmission electron microscopy (TEM, Talos F200X) equipped with energy-dispersive X-ray spectroscopy (EDS). High-angle annular dark-field scanning transmission electron microscopy (HAADF-STEM) images were taken using an FEI Titan Cubed G2 microscope equipped with a probe corrector operated at 300 kV. Inductively coupled plasma atomic emission spectroscopy (ICP-OES) analysis was recorded on a Thermo iCAP RQ instrument. N_2 adsorption/desorption isotherms were measured on a Tristar II 3020 Micromeritics analyzer. Pore volumes and sizes were computed by a quenched solid DFT method, and specific surface areas were discerned by the Brunauer–Emmett–Teller (BET) method. Atomic force microscopy (AFM) images were collected in tapping mode under ambient atmosphere using a Bruker microscope (Dimension icon) and processed with NanoScope Analysis software.

X-ray absorption data collection, analysis, and modeling

X-ray absorption fine structure spectroscopy (XAFS) measurements were carried out at the BL14W1 station in Shanghai Synchrotron Radiation Facility (SSRF, 3.5 GeV, 250 mA maximum, Si(311) double crystals). The Rh *K*-edge spectra of the Rh-SA/$Ti_3C_2O_x$ catalysts were collected in fluorescent mode using a seven-element Ge detector. Reference spectra were recorded in transmission mode using an ionization chamber. The raw data were then background-subtracted, normalized, and Fourier-transformed by the standard procedures with the ATHENA program. The least-squares curve fitting analysis was carried out using the ARTEMIS program. The data were fitted in *R*-space with theoretical models constructed on the basis of the crystal structure derived from XRD or DFT optimization.

Electrode Preparations

The preparation of the working electrodes containing the investigated catalysts can be found as follows: the rotating disk electrode (RDE, 0.19625 cm^2) was polished with alumina slurry and rinsed with distilled water before and after the catalyst was loaded on the disk. The catalyst ink was prepared by mixing 6 mg of catalyst powder, 0.5 ml of Nafion (0.05 wt.%) solution, and 0.5 ml of absolute ethyl alcohol. The mixed solution was sonicated for 1 h to form homogeneous catalytic ink. Finally, 20 μL of the catalyst ink was dropped on the glassy carbon electrode. After dried at ambient conditions, the catalyst with a content of 0.12 mg was loaded on the working electrode. As a comparison, commercial Pt/C (20 wt.%) catalyst ink was also prepared with the same method.

Electrochemical Measurements

The electrochemical measurements were carried out on the CHI 760E workstation (CH Instruments, Inc.) with a Pine rotating disk electrode system (Pins Instruments Co. Ltd.). A typical three-electrode system was employed for all of the electrochemical measurements, using a glass carbon rotating disk electrode covered by catalyst as the working electrode. A graphite rod was used as the counter electrode. An Ag/AgCl electrode saturated with KCl solution was used as the reference electrode for HER, while Hg/HgO electrode was used for HzOR. For HER, 0.1 M H_2SO_4, 1 M PBS, and 0.1 M KOH solutions were chosen as electrolytes, while 0.1 M KOH + 0.1 M N_2H_4 solution was used as the HzOR electrolyte. For HER and HzOR tests in the three-electrode system, the mass loading of the catalyst was controlled as 0.12 mg. Before all electrochemical measurements, the electrolyte was degassed for 30 min in advance with a high-purity Ar (99.999%), and a continuous flow of Ar was maintained throughout all the tests.

The recorded current density corresponds to the geometric surface area of the rotating disk electrode. All measured potentials were calibrated by 90% *iR*-compensation and adjusted to the reversible hydrogen electrode (RHE) according to the Nernst equation potential:

$$E\ (\text{V vs RHE}) = E\ (\text{V vs Ag/AgCl}) + 0.0591 \times \text{pH} + 0.197$$

$$E \text{ (V vs RHE)} = E \text{ (V vs Hg/HgO)} + 0.059 \times \text{pH} + 0.098$$

The hydrogen evolution reaction (HER) and hydrazine oxidation reaction (HzOR) activity were evaluated by using linear sweep voltammetry (LSV) with a sweep rate of 10 mV s^{-1}. The scan rate was 50 mV s^{-1} for long-term cyclic voltammetry (CV) tests. The long-term stability was tested at controlled current densities.

All the electrochemical measurements for overall hydrazine splitting (OHzS) were performed at 25 °C in a two-electrode system powered by CHI 760E electrochemical workstation with 1 M KOH + 0.1 M N_2H_4 electrolyte. The cathode chamber and anode chamber were separated by a Nafion membrane. For each pair of OHzS electrodes, the anode and the cathode were prepared by dropping the catalyst ink on carbon paper.

The electrochemical impedance spectroscopy (EIS) measurements were performed in the frequency range from 0.1 Hz to 100 kHz with an AC amplitude of 5 mV. The electrochemically active surface area (ECSA) could be examined through the electrochemical double-layer capacitance (C_{dl}). The C_{dl} can be evaluated by cyclic voltammetry in a non-Faradaic region at various scan rates. Accordingly, a series of CV measurements were conducted with 10 mV s^{-1}, 20 mV s^{-1}, 30 mV s^{-1}, 40 mV s^{-1}, and 50 mV s^{-1} in 0.1 to 0.2 V vs RHE. The double-layer capacitance values were determined from the slope of the capacitive current versus scan rate.

The current density normalized by electrochemical active surface area was calculated using the following equation:

$$J_{ECSA} = I / S_{ECSA}$$

where J_{ECSA} is the current density normalised by ECSA (mA cm^{-2}), I is the current (mA), $S_{ECSA} = C_{dl} / C_s$ (C_s = 0.035 mF cm^{-2}).

Determine H_2 Faradaic Efficiency

The experimental amounts of H_2 evolved from the cathode during the hydrogen evolution reaction could be measured by the drainage gas collection method. The theoretical volume of H_2 was calculated from the following relationships:

$$V_{H2}\ (\text{mL}) = Q \times 22.4\ \text{L mol}^{-1} \times 1000 / (\text{F} \times 2)$$

where Q is the cumulative charge (C), F is the Faraday constant (96,485 C mol^{-1}).

The Faradic efficiency (FE) was calculated using the following equation:

$$\text{FE} = \frac{\text{Experimental μmol of gas}}{\text{Theoretical μmol of gas}} \times 100\%$$

As for the theoretical quantity, the efficiency of the current produced by the reactions was assumed to be 100 %, which in turn assumes that HER is the only reaction that takes place on the respective electrode.

Determine N_2H_4 decomposition

To determine whether hydrazine decomposes to form the mixture products of N_2 and H_2 ($N_2H_4 \rightarrow N_2 + 2H_2$) in alkaline solution, the gas products in the control experiments were collected and analyzed by an online gas chromatograph. The control experiment was performed as the following: Firstly, approximately 10 mg of the as-prepared catalyst was added into a three-necked round bottom flask. The 1 M KOH + 0.1 M N_2H_4 aqueous solution was rapidly injected into the flask with magnetic stirring. A stream of Ar continues to flow through the flask to bring the possible gas products into the gas chromatograph for the qualitative analysis.

TOF Calculations

The turnover frequency (TOF) calculation values of the designed catalysts were measured and calculated according to the following equation:

$$\text{TOF} = \frac{j}{z \times \text{F} \times n}$$

where j is the HER current density (A cm^{-2}) during the LSV measurement in 0.1 M H_2SO_4 solutions, z represents the electron number per mol involved to generate a mole of H_2 (z = 2) in HER. F is the Faraday constant (96,485 C mol^{-1}), and n is the number of active sites.

The n values can be approximately estimated by CV measurements carried out in 1 M PBS electrolyte (pH = 7) with a scan rate of 50 mV s^{-1} at the potential window from −0.2 to 0.6 V vs. RHE for HER. After this, by integrating the charge of each CV curve over the whole potential range, the half value of the charge was obtained, which is the value of the surface charge density (Q_s). Then, the n value was computed by $n = Q_s/F$.

Assembly and Tests of Zn-H_2 Battery

The asymmetric Zn-H_2 battery was assembled of carbon paper (1 × 1 cm^2) supported Rh-SA/$Ti_3C_2O_x$ with a mass loading of 1 mg cm^{-2} as the cathode, A polished Zn plate as the anode, and 2.0 M H_2SO_4 and 4.0 M NaOH as the catholyte and anolyte, respectively. A bipolar membrane (BPM) was used as a separator for preventing bulk neutralization of acidic catholyte and alkaline anolyte. For comparison, the commercial 20 wt% Pt/C catalysts were also measured under the same conditions. The polarization curve measurements were performed by LSV at 10 mV s^{-1}. The rate discharging curves and long-time durability test were collected by the electrochemical workstation testing system. Both the current density and power density were normalized to the geometric area of the cathode. For galvanostatic discharge results, the specific capacity (C) and energy density (E) were calculated as follows:

$$C = I \times t/m$$

$$E = I \times V \times t/\mathrm{m}$$

where I is the applied current, V is the average discharge voltage, t is the service hours, and m is the weight of the consumed Zn plate.

Calculation of Theoretical Potential of the Zn-H_2 battery

When discharging, the reaction pathways of the acid-alkaline Zn-H_2 battery can be expressed as follows according to the Nernst equation:

Hydrogen evolution reaction at the cathode (2.0 M H_2SO_4):

$$2H^+ + 2e^- \rightarrow H_2$$

$$E_c = E^{\theta}_{H^+/H_2} + 2.303\frac{RT}{2F}log\left[\frac{\alpha_{H_2}}{(\alpha_{H^+})^2}\right] = 0\ V + 0.059 \times \log\left(\alpha_{H^+}\right) = 0.035\ V$$

where $E^{\theta}_{H^+/H_2} = 0\ V\ vs\ SHE$.

Oxidation of Zn at the anode (4.0 M NaOH):

$$Zn - 2e^- + 2OH^- \rightarrow H_2O + ZnO$$

$$E_a = E^{\theta}_{\frac{Zn^{2+}}{Zn}} - 2.303\frac{RT}{2F}log\left[\left(\alpha_{OH^-}\right)^2\right] = -1.249\ V - 0.059 \times \log\left(\alpha_{OH^-}\right) = -1.285\ V$$

where $E^{\theta}_{Zn^{2+}/Zn} = -1.249\ V\ vs\ SHE$.

The overall reaction:

$$Zn + 2H^+ + 2OH^- \rightarrow H_2 + H_2O + ZnO$$

The theoretical electromotive force (E_{emf}) of the battery could be:

$$E_{emf} = E_c - E_a$$

$$= E^{\theta}_{\frac{H^+}{H_2}} - 2.303\frac{RT}{2F}log\left[\frac{\alpha_{H_2}}{\left(\alpha_{H^+}\right)^2}\right] - \left\{E^{\theta}_{\frac{Zn^{2+}}{Zn}} - 2.303\frac{RT}{4F}log\left[\left(\alpha_{OH^-}\right)^2\right]\right\}$$

$$= E^{\theta}_{\frac{H^+}{H_2}} - E^{\theta}_{\frac{Zn^{2+}}{Zn}} + 0.059 \times \left[\log\left(\alpha_{H^+}\right) + \log\left(\alpha_{OH^-}\right)\right] = 1.32\ V$$

where R is the gas constant (8.314 J mol^{-1} K^{-1}), F is the faraday constant (96,485 C mol^{-1}), T is 298.15 K, and α is the corresponding activity.

Calculation of Theoretical Energy Density of the Zn-H_2 battery

The theoretical energy density of the Zn-H_2 battery could be:

$$ED_{theo} = C_{theo}V_{cell} = 820\ mAh\ g^{-1} \times 1.32\ V = 1082.4\ Wh\ kg^{-1}$$

where C_{Zn} is the theoretical capacity of the battery based on Zn anode.

Assembly and Tests of Self-Powered Dual Hydrogen Production System

The self-powered dual hydrogen production system was consisted of integrating a Zn-H_2 battery using Rh-SA/$Ti_3C_2O_x$ cathode and Zn plate as the anode to drive OHzS for H_2 production. In this system, hydrogen could be generated simultaneously from two pathways: the cathode of the Zn-H_2 unit and the cathode of the OHzS. The experimental amounts of H_2 evolved from the cathode during the hydrogen evolution reaction could be measured by the drainage gas collection method.

Computational Details

All calculations were performed with dispersion-corrected DFT in the DMol^3 code. The starting models of pristine MXene Ti_3C_2 were constructed conventionally by removing Al sheets from the parent MAX phase Ti_3AlC_2. The two-dimension material consists of five (Ti_3C_2) atomic sheets with a hexagonal-like unit cell. The atomic models of the functionalized MXenes were designed assuming their complete surface termination by oxygen atoms. The periodic system had a vacuum thickness of 15 Å, which was used to eliminate spurious interactions between the adsorbate and the periodic image of the bottom layer of the surface. All the computations were performed with spin-polarized DFT implemented in the DMol^3 code of the Materials Studio. A generalized gradient approximation (GGA) with the Perdew, Burke, and Ernzerhof (PBE) exchange-correlation functionals was employed. The double numerical plus polarization (DNP) was used as the basis set. Effective core potentials were adopted as the core treatment to conduct a metal relativistic effect. The geometry convergence tolerance for energy change was 1×10^{-6} Ha, the max force was 0.002 Ha/Å, and the max displacement was 0.005 Å. We chose 5.2 Å to be the real-space global orbital cutoff radius. The structural optimization was performed without any constraints. The Gibbs free energy change (ΔG) of each elemental step was calculated according to the CHE model, which used one-half of the chemical potential of hydrogen as the chemical potential of the proton-electron pairs. ΔG was calculated by the equation: $\Delta G = \Delta E + \Delta E_{ZPE} + \Delta G_U - T\Delta S$, where ΔE is the electronic energy difference directly obtained from DFT

calculations, ΔE_{ZPE} is the zero-point energy, T is the temperature (T = 298.15 K), ΔS is the change in entropy, and ΔG_U is the free energy contributions related to the applied electrode potential U.

Supplementary Figures

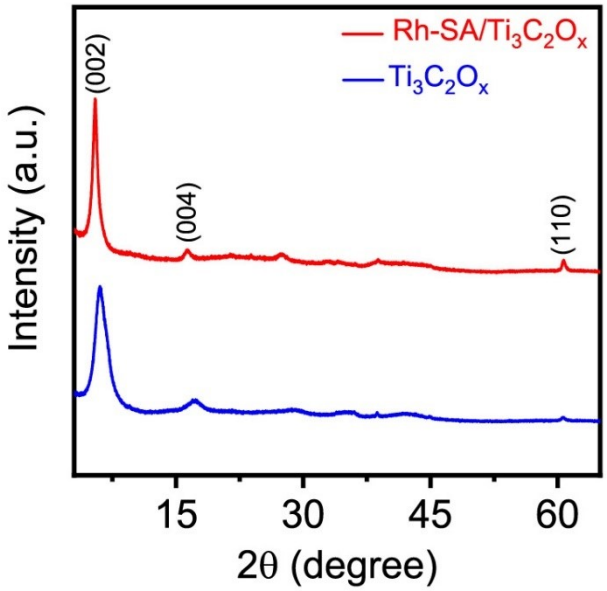

Figure S1. XRD patterns of the as-prepared Rh-SA/$Ti_3C_2O_x$ and $Ti_3C_2O_x$ samples.

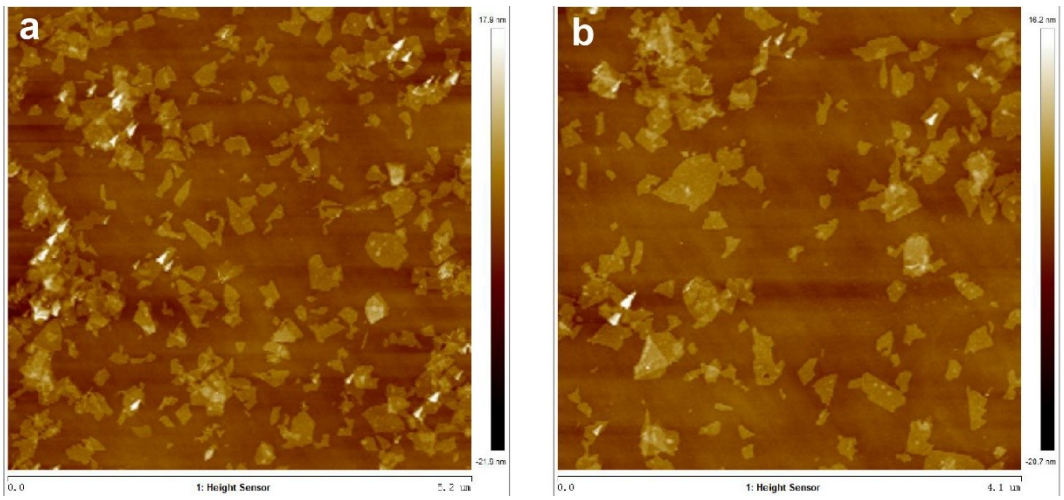

Figure S2. The additional AFM images of the as-prepared Rh-SA/$Ti_3C_2O_x$ sample.

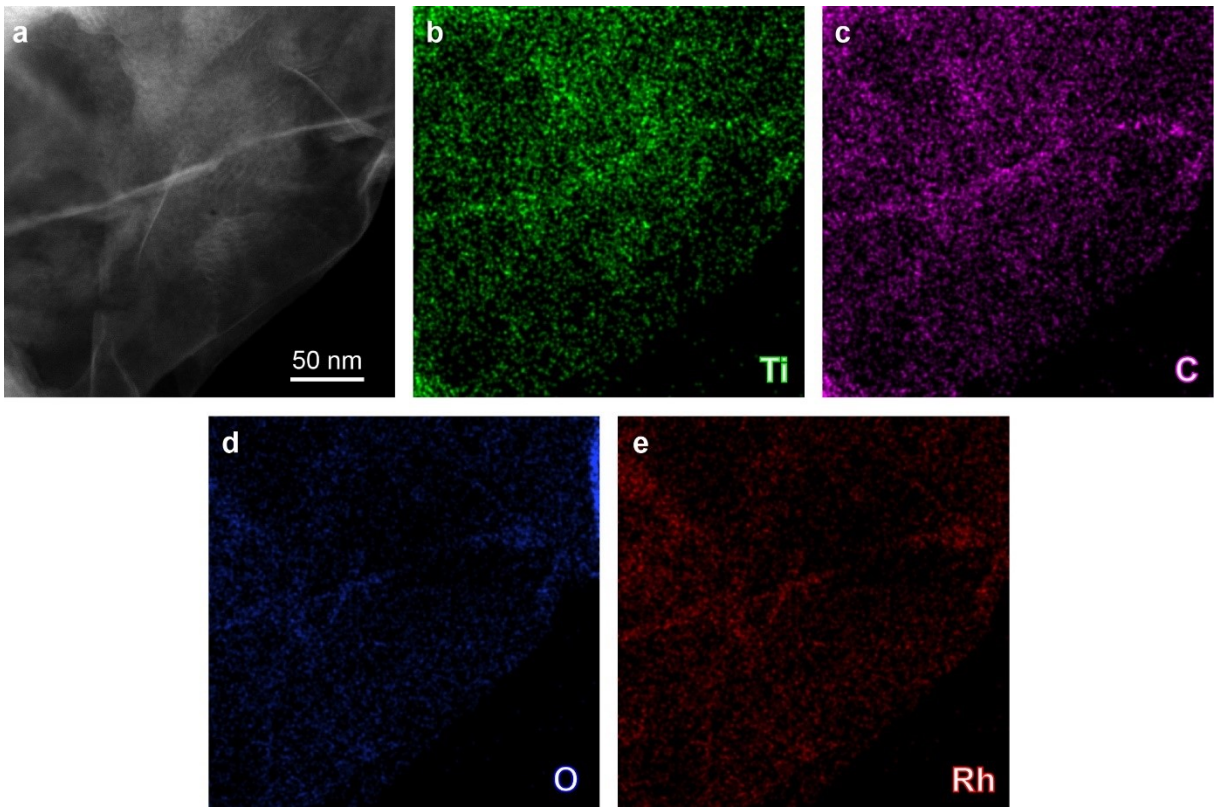

Figure S3. The EDS mapping characterization of the as-prepared Rh-SA/$Ti_3C_2O_x$ sample. (a) HAADF-STEM image, (b-e) the corresponding EDS element mapping. From the HAADF-STEM image, the Rh nanoclusters or nanoparticles cannot be observed. The EDS elemental mapping confirms the homogeneous distribution of these elements in the composite.

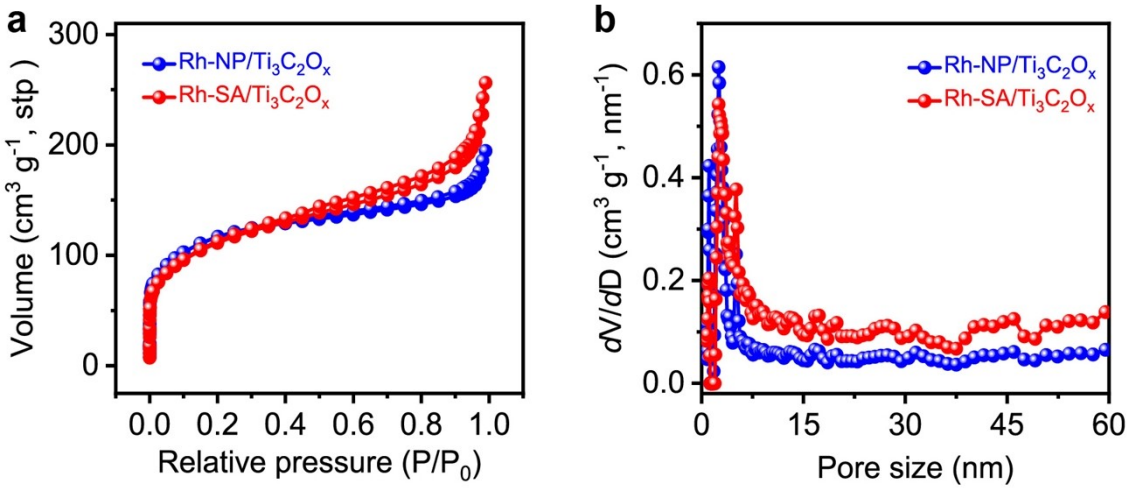

Figure S4. The BET measurements of the as-prepared Rh-NP/$Ti_3C_2O_x$ and Rh-SA/$Ti_3C_2O_x$ samples. (a) N_2 adsorption/desorption isotherm curves. (b) The corresponding pore size distribution. The pore structure and specific surface areas properties of the as-prepared samples were characterized by N_2 adsorption/desorption measurements. As result, the as-synthesized Rh-SA/$Ti_3C_2O_x$ nanosheets possess a specific surface area of 441.81 $m^2\ g^{-1}$ with a pore volume of 0.333 $cm^3\ g^{-1}$. Moreover, the Rh-SA/$Ti_3C_2O_x$ sample showed a prominent pore size distribution around 2.5 nm. Besides, Rh-NP/$Ti_3C_2O_x$ (Specific surface areas: 416.61 $m^2\ g^{-1}$; Pore volume: 0.397 $cm^3\ g^{-1}$; Prominent pore size: 2.5 nm) exhibited a similar pore structure and specific surface areas properties to that of Rh-SA/$Ti_3C_2O_x$, which provides higher comparability for the electrochemical performance comparison of Rh-SA/$Ti_3C_2O_x$ and Rh-SA/$Ti_3C_2O_x$.

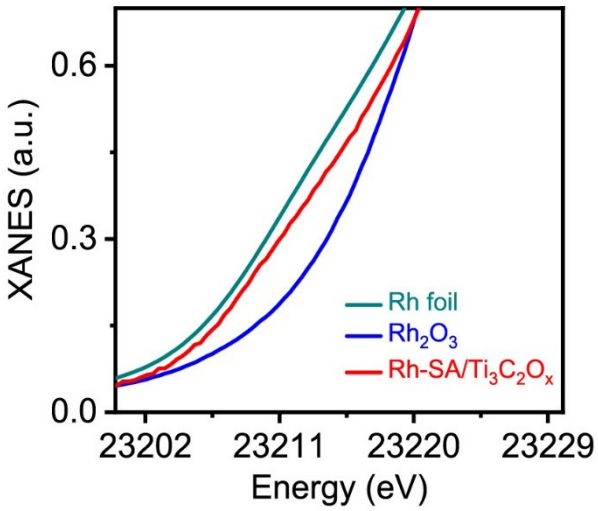

Figure S5. The detailed view of Rh *K*-edge XANES curves of Rh-SA/$Ti_3C_2O_x$, as well as Rh foil and Rh_2O_3 references. Clearly, the absorption edge position of the white line for Rh-SA/$Ti_3C_2O_x$ was located between those of Rh foil and Rh_2O_3, indicating that the valence state of Rh single atoms is situated between that of Rh^0 and Rh^{+3}.

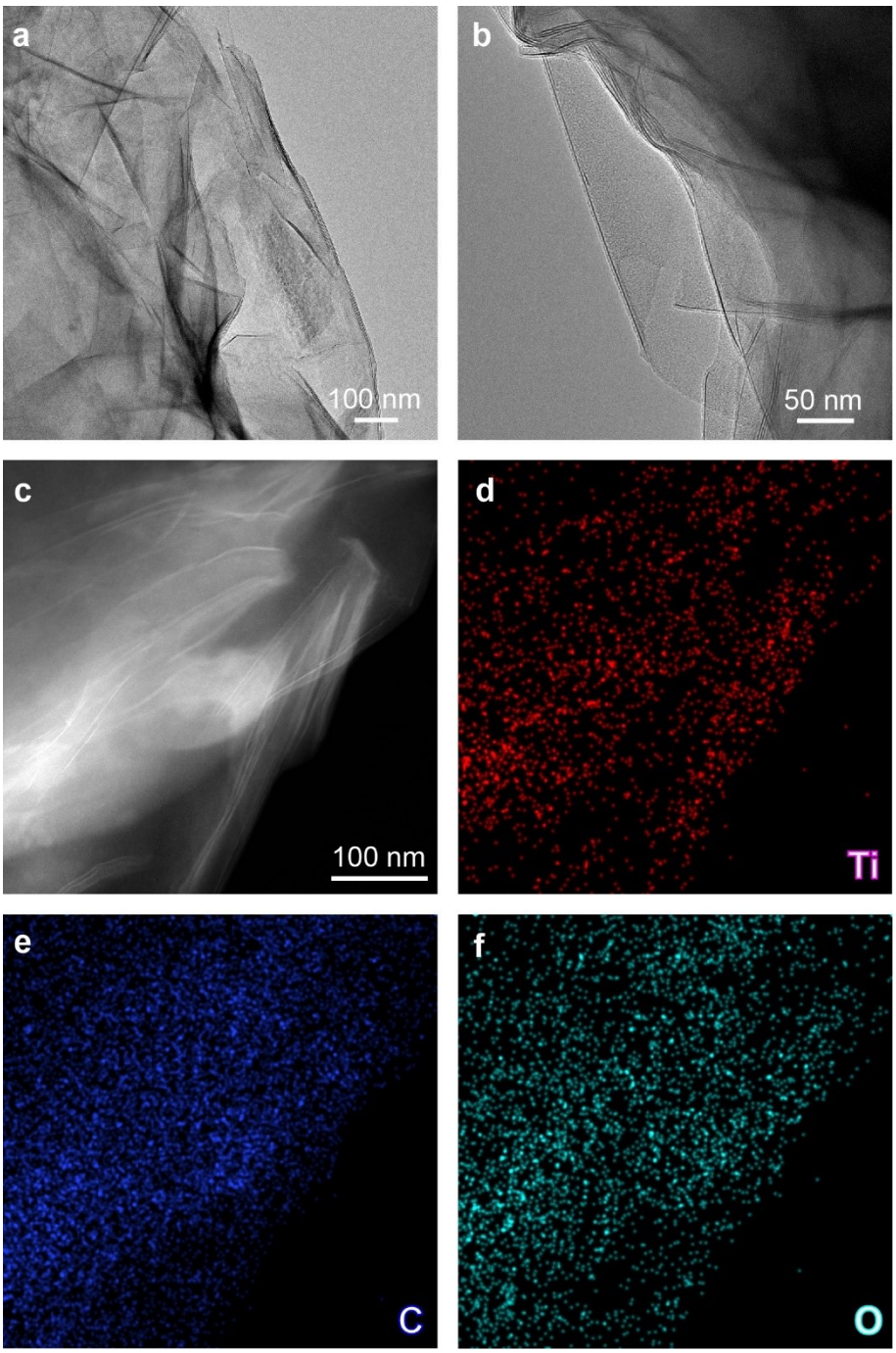

Figure S6. The morphology and EDS mapping characterizations of the as-prepared $Ti_3C_2O_x$ sample. (a,b) TEM images. (c) HAADF-STEM image. (d-f) EDS element mapping corresponding to (c). From the TEM images, the $Ti_3C_2O_x$ displayed ultrathin nanosheet morphology with a few layers. The EDS elemental mapping confirms the homogeneous distribution of these elements in the composite.

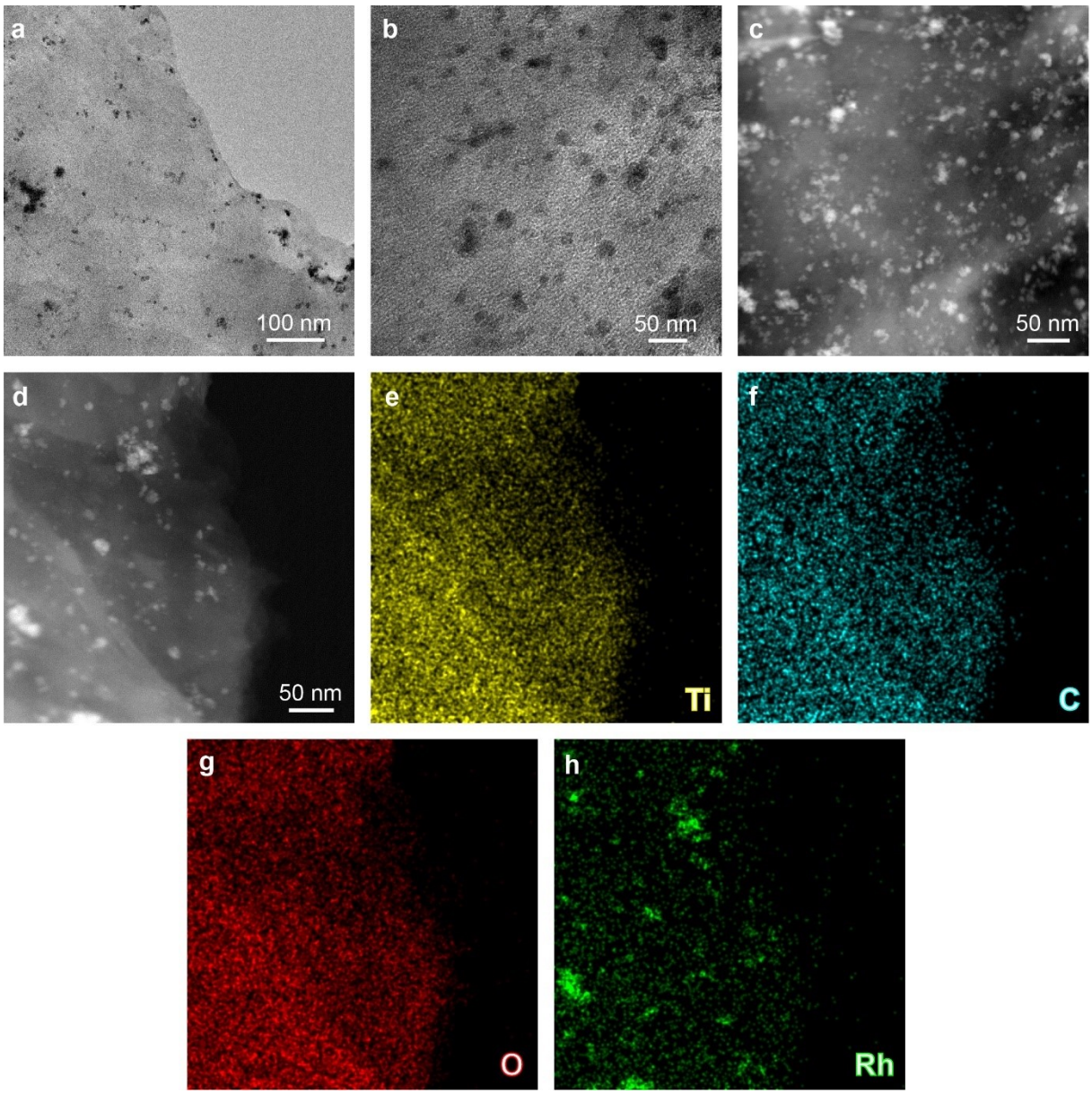

Figure S7. The morphology and EDS mapping characterizations of the as-prepared Rh-NP/$Ti_3C_2O_x$ sample. (a,b) TEM images. (c,d) HAADF-STEM images. (e–h) EDS element mapping corresponding to (d). From the TEM images, the Rh nanoparticles can be clearly observed. The EDS elemental mapping confirms the homogeneous distribution of these elements in the composite. The Rh loading was determined to be 3.75 wt.% by ICP-OES analysis.

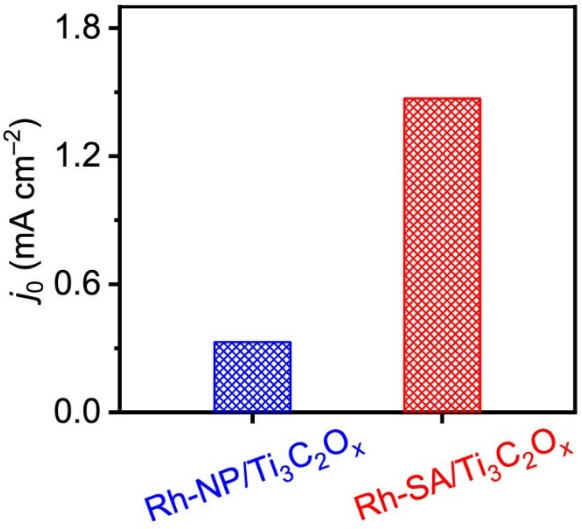

Figure S8. The exchange current densities (j_0) of the Rh-NP/$Ti_3C_2O_x$ and Rh-SA/$Ti_3C_2O_x$ catalysts. As shown, the value of j_0 of the Rh-SA/$Ti_3C_2O_x$ catalyst was 1.57 mA cm^{-2}, which was much higher than Rh-NP/$Ti_3C_2O_x$ (0.33 mA cm^{-2}) and those of most previously reported HER electrocatalysts (**Table S3**, Supporting Information)), suggesting a more rapid HER rate and an additional kinetic advantage for Rh-SA/$Ti_3C_2O_x$.

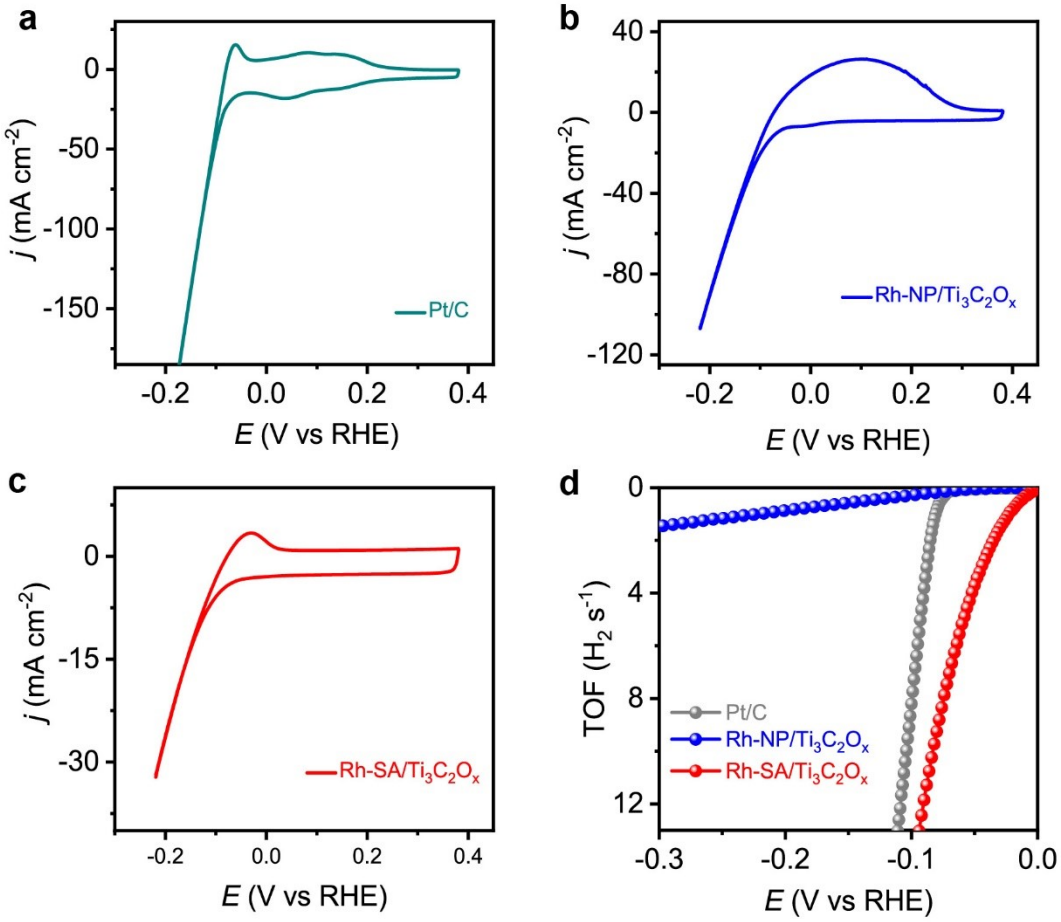

Figure S9. Determination of active sites and TOF values for HER. (a) HER CV curves of Pt/C. (b) HER CV curves of Rh-NP/$Ti_3C_2O_x$. (c) HER CV curves of Rh-SA/$Ti_3C_2O_x$. (d) TOF plots for HER.

By the curves in (a) here (see more details in Methods), the Q_s values of Pt/C, Rh-NP/$Ti_3C_2O_x$, and Rh-SA/$Ti_3C_2O_x$ were measured to be 3.986×10^{-2}, 4.568×10^{-2}, and 0.971×10^{-3} C cm^{-2}, respectively. Thus, their corresponding *n* values under HER conditions were calculated to be 4.131×10^{-8}, 4.766×10^{-8}, and 1.006×10^{-8} mol cm^{-2}, respectively. Based on the above results, the TOF values were calculated and plotted in **d**. As shown, Rh-SA/$Ti_3C_2O_x$ exhibited a larger TOF value, indicating its higher intrinsic activity than those of the counterparts.

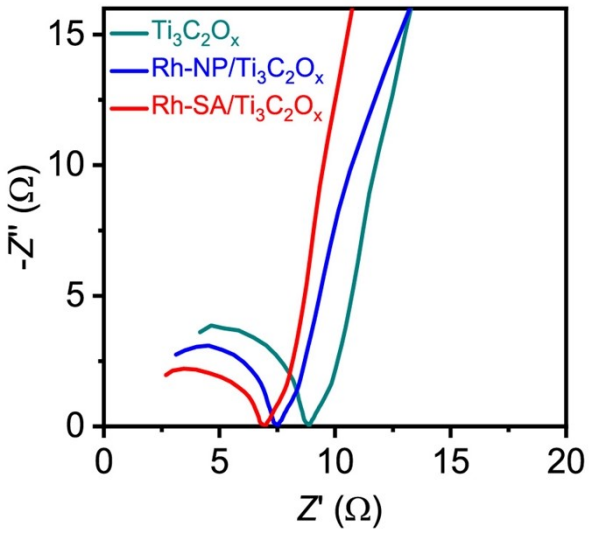

Figure S10. Nyquist plots of the $Ti_3C_2O_x$, Rh-NP/$Ti_3C_2O_x$, and Rh-SA/$Ti_3C_2O_x$ electrodes.

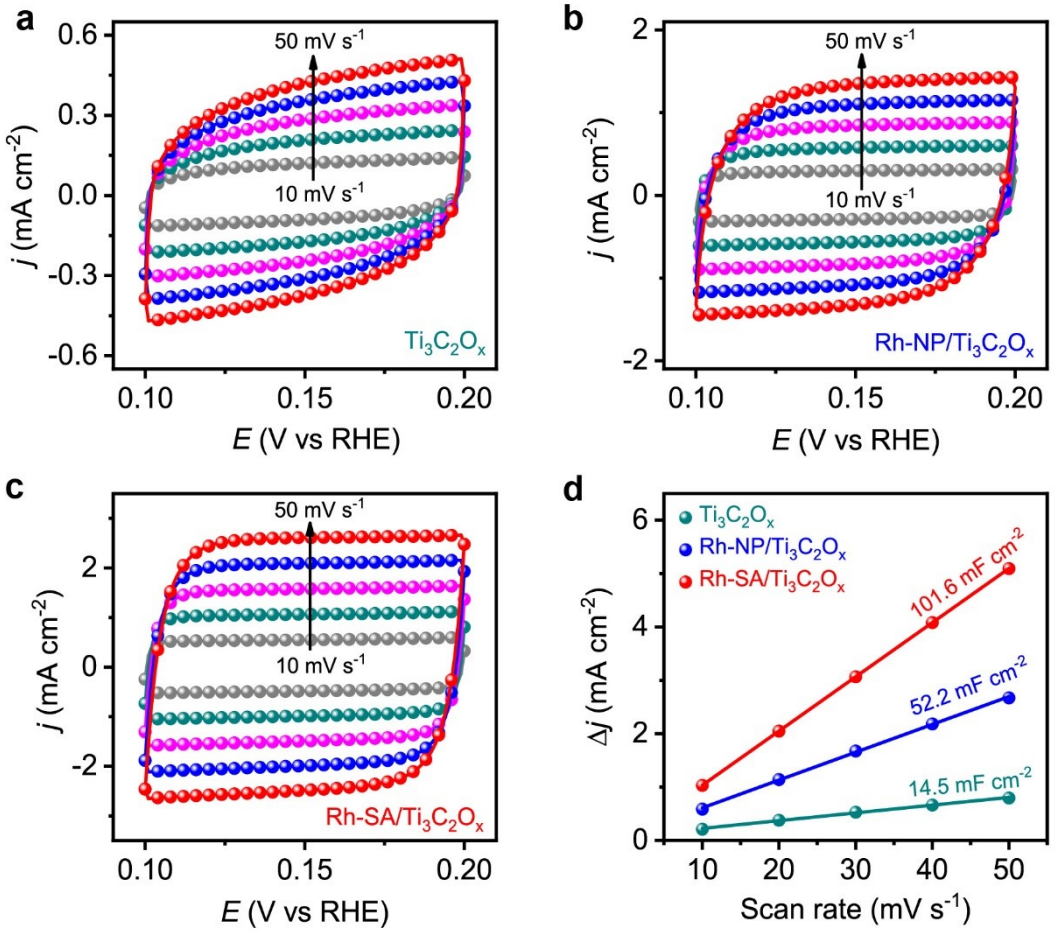

Figure S11. The determination of C_{dl}. (a–c), CV curves of $Ti_3C_2O_x$ in (a) and Rh-NP/$Ti_3C_2O_x$ in (b) and Rh-SA/$Ti_3C_2O_x$ in c, which has been measured in 0.1 M H_2SO_4 aqueous electrolyte with various scan rates of 10, 20, 30, 40, and 50 mV s^{-1} in the non-faradaic region. (d) The capacitive current densities as a function of scan rate for the different catalysts.

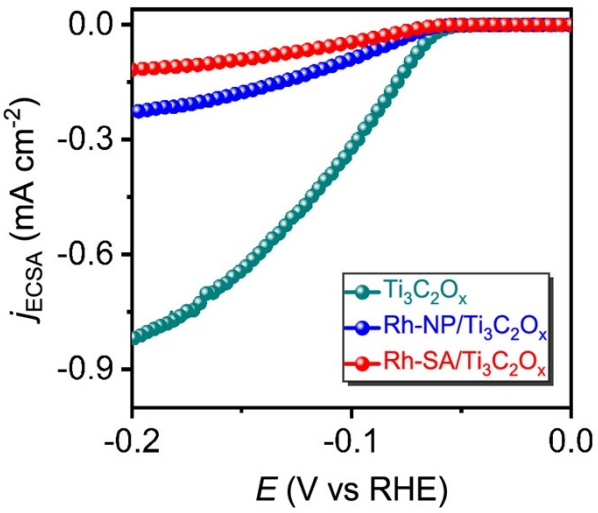

Figure S12. ECSA normalized polarization curves recorded at a scan rate of 10 mV s^{-1} in 0.1 M H_2SO_4 aqueous solution.

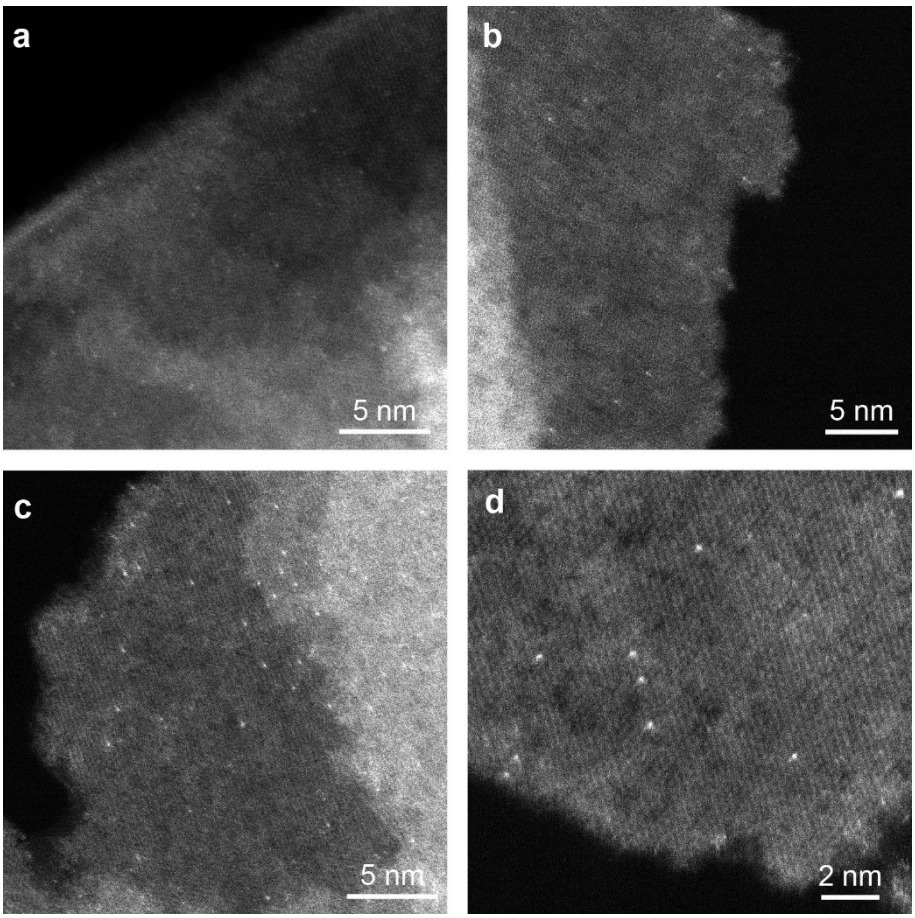

Figure S13. The atomic-resolution HAADF-STEM images of Rh-SA/$Ti_3C_2O_x$ after HER stability test with 5,000 continuous cyclic voltammetry cycles. These images were taken from randomly selected regions of the sample. As seen, no clusters and particles could be observed on the surface of the Rh-SA/$Ti_3C_2O_x$ nanosheets after the stability test, further excluding the possible formation of Rh nanoclusters or nanoparticles, confirming its robust structural stability during the HER process.

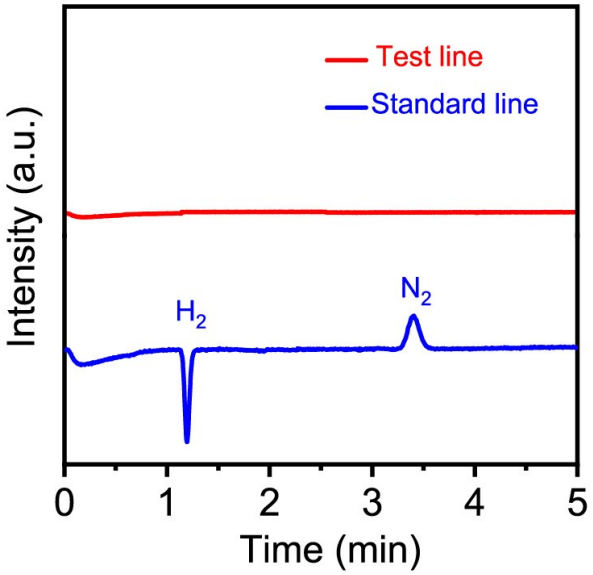

Figure S14. The control experiments for determining the possible gas products from the direct N_2H_4 decomposition. The blue curve is the standard line containing N_2 and H_2, and the red curve is the test line of the control experiment. As shown, no N_2 and H_2 were detected in the control experiment, confirming the Rh-SA/$Ti_3C_2O_x$ catalyst cannot catalyze the direct decomposition of hydrazine in alkaline solution.

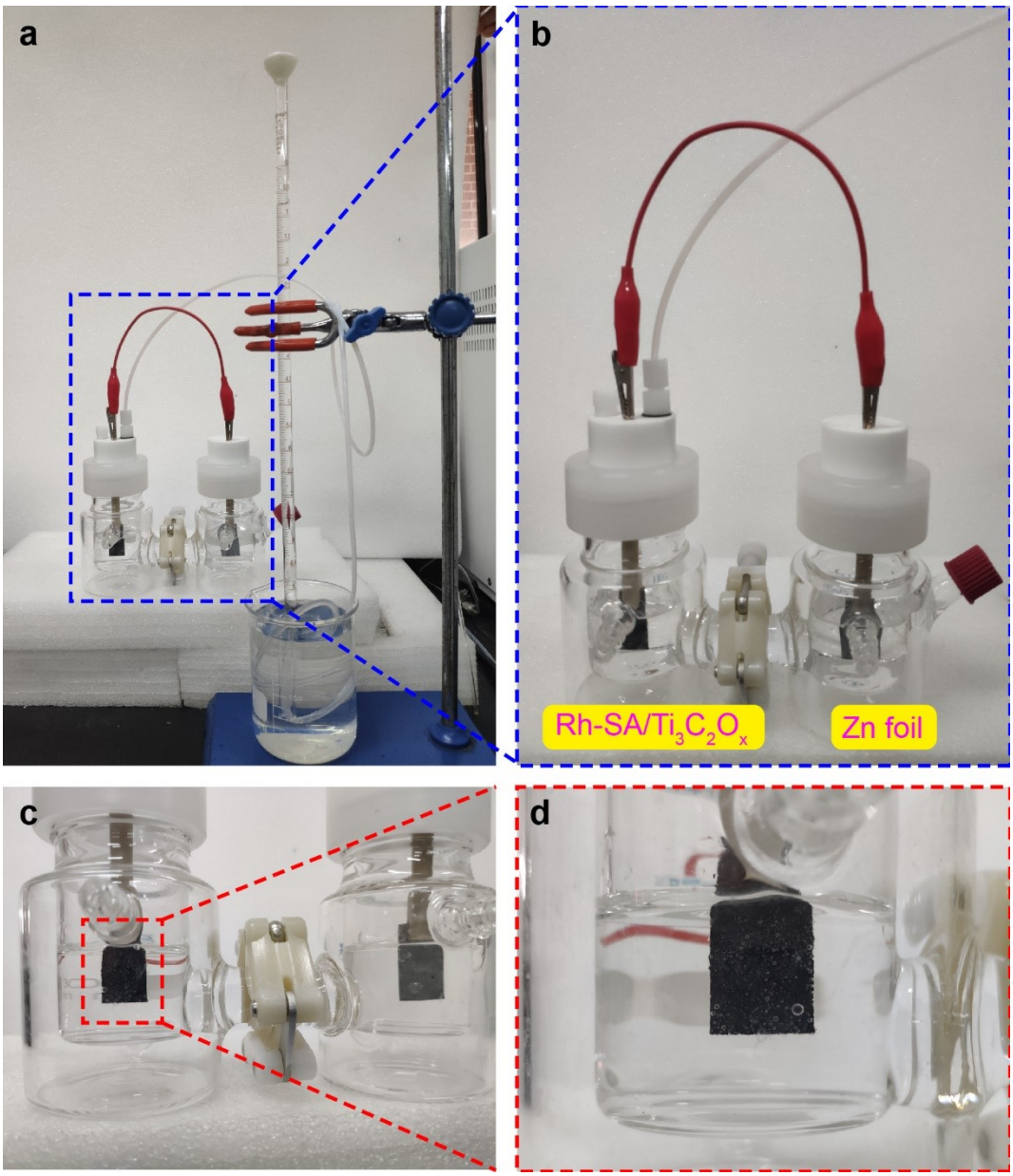

Figure S15. The digital photograph of the homemade gas collection device for the Zn-H_2 battery system.

The enlarged view in (d) displayed the generated hydrogen bubbles over the Rh-SA/$Ti_3C_2O_x$ electrode.

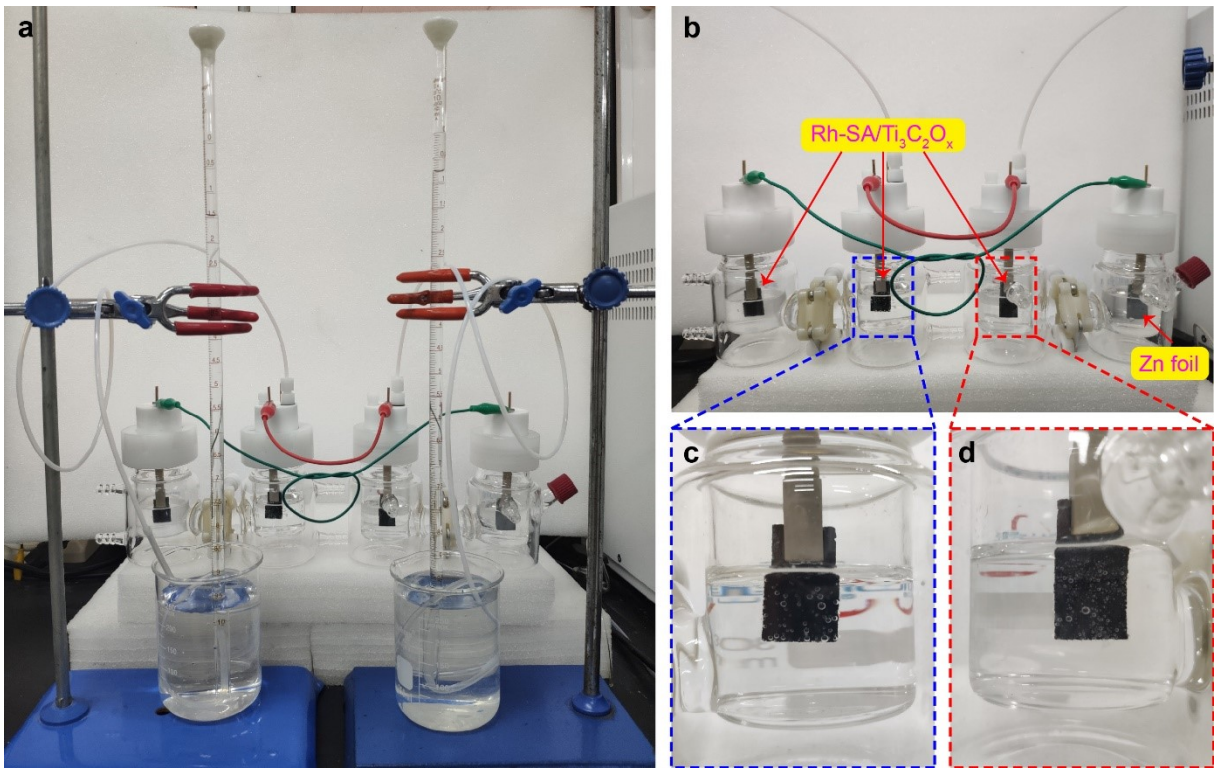

Figure S16. The digital photograph of the homemade gas collection device for the self-powered dual hydrogen production system. The enlarged view in (c) and (d) displayed the generated hydrogen bubbles over the cathode of the OHzS (c) and the Zn-H_2 battery (d), respectively.

Supplementary Tables

Table S1. The structural parameters extracted from the Rh *K*-edge EXAFS fitting for the Rh-SA/$Ti_3C_2O_x$ sample.

Sample	Bond type	*N*	*R*(Å)	$\sigma^2(10^{-3}$ Å$^2)$	ΔE_0(eV)	*R* factor
Rh-SA/$Ti_3C_2O_x$	Rh-O	3	2.07 ± 0.05	0.0054	-5.477	0.0029
	Rh-Ti	3	2.13 ± 0.03	-0.0005	-5.477	

S_0^2 is the amplitude reduction factor; *N* is the coordination number; *R* is the interatomic distance (the bond length between central atoms and surrounding coordination atoms); σ^2 is Debye-Waller factor (a measure of thermal and static disorder in absorber-scatterer distances); ΔE_0 is an edge-energy shift (the difference between the zero kinetic energy value of the sample and that of the theoretical model). *R* factor is used to value the goodness of the fitting.

Table S2. Comparison of the HER performance of Rh-SA/$Ti_3C_2O_x$ with previously electrocatalysts in acidic conditions.

Catalysts	*Electrolyte*	*η_{10}* (mV vs RHE)	*Tafel* (mV dec^{-1})	*Stability*	*References*
Rh-SA/$Ti_3C_2O_x$	0.1 M H_2SO_4	23	27.8	24 h + 5,000 CV cycles	This work
B-CoP/CNT	0.5 M H_2SO_4	39	50	100 h	Angew. Chem. Int. Ed. 2020, 59, 4154
CoP/NPC/TF	0.5 M H_2SO_4	91	54	10 h	Adv. Energy Mater. 2019, 9, 1803970
Ce, N-CoP/CC	0.5 M H_2SO_4	66	53	60 h	Sustain. Energy Fuels, 2019, 3, 3344
CeO_2/Co_4N	0.5 M H_2SO_4	33	65	12 h	Appl. Catal. B-Environ. 2020, 277, 119282
Co@NG/NRGO	0.5 M H_2SO_4	91	62	36 h	Chem. Commun., 2020, 56, 567
$Co_{0.31}Mo_{1.69}C$/MXene/NC	0.5 M H_2SO_4	81	24	100 h	Adv. Energy Mater. 2019, 9, 1901333
N-Co-S/G	0.5 M H_2SO_4	67.7	56.3	100 h	Nano Energy 2021, 80, 105544
Co-P@PC-750	0.5 M H_2SO_4	72	49	20 h	Small 2020, 16, 1900550

CoP-400	0.5 M H_2SO_4	113	67	70,000 s	Small 2018, 14, 1802824
CoP/Ni_2P@HPNCP	0.5 M H_2SO_4	130	64.91	20 h	Nanoscale, 2020, 12, 23851
CoS_2@MoS_2@CC-30h	0.5 M H_2SO_4	65	122	20 h	Adv. Mater. Interfaces 2020, 7, 2000780
Cu@WC	0.5 M H_2SO_4	92	50.5	12 h	Appl. Catal. B-Environ. 2021, 280, 119451
$Cu_{0.075}Co_{0.925}P$/CP	0.5 M H_2SO_4	47	47.2	24 h	J. Mater. Chem. A, 2019, 7, 14271
N_V-Fe_2N-350	0.5 M H_2SO_4	54	41.2	50 h	Adv. Mater. 2020, 32, 1904346
FeP/NCNSs	0.5 M H_2SO_4	114	64	20 h	ACS Sustainable Chem. Eng. 2018, 6, 11587
FeP/Ti	0.5 M H_2SO_4	79	58	10 h	Appl. Catal. B-Environ. 2020, 260, 118156
$Fe_{0.43}Co_{2.57}(PO_4)_2$/Cu	0.5 M H_2SO_4	63.8	42.4	100 h	ACS Sustainable Chem. Eng. 2020, 8, 13793
CoP/CC	0.5 M H_2SO_4	67	51	22.5 h	J. Am. Chem. Soc. 2014, 136, 7587
FeP/C	0.5 M H_2SO_4	71	52	10,000 CV cycles	J. Am. Chem. Soc. 2017, 139, 6669

CoP/CNT	0.5 M H_2SO_4	122	54	18 h	Angew. Chem. Int. Ed. 2014, 53, 6710
Co_2P@N,P-PCN/CNTs	0.5 M H_2SO_4	126	45	25 h	J. Mater. Chem. A 2016, 4, 15501
Co-Ni-P/NF	0.5 M H_2SO_4	68	56.4	40 h	Catal. Today 2017, 287, 122
Co phosphide/phosphate thin film	0.5 M H_2SO_4	150	53	13.9 h	Adv. Mater. 2015, 27, 3175
Urchin-like CoP/GC	0.5 M H_2SO_4	105	46	30 h	Nano Lett. 2015, 15, 7616
Fe-Co_2P/NCNTs	0.5 M H_2SO_4	104	58	16.7 h	ACS Appl. Mater. Interfaces 2016, 8, 13890
CoMoP@C/GC	0.5 M H_2SO_4	41	49.7	24 h	Energy Environ. Sci. 2017, 10, 788
Co_2P nanorods/Ti	0.5 M H_2SO_4	134	71	12 h	Nano Energy 2014, 9, 373
CoPS/GE	0.5 M H_2SO_4	128	57	36 h	Nat. Mater. 2015, 14, 1245
rGO-few layer $FePS_3$	0.5 M H_2SO_4	108	54	50 h	ACS Energy Lett. 2016, 1, 367
Se-rich $MoSe_2$	0.5 M H_2SO_4	130	46	12 h	ACS Nano 2020, 14, 6295

Mo-WC@NCS	0.5 M H_2SO_4	155	78	12 h	Nano Energy 2020, 74, 104850
CoP NW/Hb	0.5 M H_2SO_4	78	68	14 h	Nano Res. 2017, 10, 1010
Ni-C-N NS	0.5 M H_2SO_4	60.9	32	70 h	J. Am. Chem. Soc. 2016, 138, 14546
C_3N_4@N-doped graphene	0.5 M H_2SO_4	240	51.5	1,000 CV cycles	Nat. Commun. 2014, 5, 3783
$NiCo_2P_x$/CF	0.5 M H_2SO_4	104	59.6	30 h	Adv. Mater. 2017, 29, 1605502
S-MoO_2-2	0.5 M H_2SO_4	176	57	1,000 CV cycles	Nano Res. 2019, 13, 121
MoS_2-C_3N_4-60	0.5 M H_2SO_4	173	53	1,000 CV cycles	J. Catal. 2019, 375, 441
$Mo_2F_xC_{1-x}$/rGO	1 M $HClO_4$	95	86	48 h	ACS Sustainable Chem. Eng. 2020, 8, 10284
Mo-Ni_2P/NF	0.5 M H_2SO_4	67	77	24 h	Nanoscale 2017, 9, 16674
MoP/CNT-700	0.5 M H_2SO_4	83	60	40 h	Adv. Funct. Mater. 2018, 28, 1706523

η_{10} is the overpotential at the current density of −10 mA cm^{-2} except those specified else.

Table S3. Comparison of the HER exchange current density (j_0) of Rh-SA/$Ti_3C_2O_x$ with previously electrocatalysts.

Catalysts	*Electrolyte*	*j_0 (mA cm^{-2})*	*References*
Rh-SA/$Ti_3C_2O_x$	0.1 M H_2SO_4	1.57	This work
Pd^0/GDY	0.5 M H_2SO_4	0.282	iScience 2019, 11, 31
MoC-Mo2C/PNCDs	1.0 M KOH	0.15	Adv. Mater. 2019, 31, 1900699
$MoNi_4$	1.0 M KOH	1.24	Nat. Commun. 2017, **8**, 15437
Mo_2C-WC	0.5 M H_2SO_4	0.419	J. Mater. Chem. A, 2017,5, 18494
	1.0 M KOH	0.804	
Ru-SA/$Ti_3C_2T_x$	0.1 M $HClO_4$	0.06	Small 2020, 6, 2002888
CoP/CC	0.5 M H_2SO_4	0.288	J. Am. Chem. Soc. 2014, 136, 7587
2H $Nb_{1.35}S_2$	0.5 M H_2SO_4	~0.8	Nat. Mater. 2019, 18, 1309

PdCu-B2 NWs	0.5 M H_2SO_4	4.7	ACS Energy Lett. 2020, 5, 3672
1% PtW_6O_{24}/C	0.5 M H_2SO_4	1.65	Nat. Commun. 2020, 11, 490
W_1Mo_1-NG	0.5 M H_2SO_4	1.78	Sci. Adv. 2020, 6, eaba6586
Mo_2-NG		1.50	
W_2-NG		0.33	
NG		0.67	
Metallic-phase MoS_2	0.5 M H_2SO_4	0.1	Nat. Commun. 2016, 7, 10672
$Pt_{3.21}Ni@Ti_3C_2$	0.1 M KOH	0.9	Small 2019, 15, 1805474
Li_xNiO/Ni	0.5 M H_2SO_4	1.1	J. Am. Chem. Soc. 2020, 142, 12613
a-Ni_3S_2@NPC	0.5 M H_2SO_4	0.492	Nano Energy 2017, 36, 85–94
	1 M KOH	0.786	

	2 M PBS	0.0428	

Table S4. Comparison of the HER performance of Rh-SA/$Ti_3C_2O_x$ with previously electrocatalysts in alkaline conditions.

Catalysts	*Electrolyte*	η_{10} (mV vs RHE)	*Tafel* (mV dec^{-1})	*Stability*	*References*
Rh-SA/$Ti_3C_2O_x$	0.1 M KOH	29	47.6	24 h	This work
B-CoP/CNT	1 M KOH	56	69	100 h	Angew. Chem. Int. Ed. 2020, 59, 4154
CoP/NPC/TF	1 M KOH	80	50	10 h	Adv. Energy Mater. 2019, 9, 1803970
Ce, N-CoP/CC	1 M KOH	41	43	60 h	Sustain. Energy Fuels, 2019, 3, 3344
CeO_2/Co_4N	1 M KOH	30	66	15 h	Appl. Catal. B-Environ. 2020, 277, 119282
Co@NG/NRGO	1 M KOH	70	64	36 h	Chem. Commun., 2020, 56, 567
$Co_{0.31}Mo_{1.69}C$/MXene/NC	1 M KOH	75	43	100 h	Adv. Energy Mater. 2019, 9, 1901333
N-Co-S/G	1 M KOH	74.5	61.9	100 h	Nano Energy 2021, 80, 105544
Co-P@PC-750	1 M KOH	76	52	20 h	Small 2020, 16, 1900550
CoP-400	1 M KOH	154	72	70,000 s	Small 2018, 14, 1802824

CoP/Ni_2P@HPNCP	1 M KOH	121	61.89	20 h	Nanoscale, 2020, 12, 23851
CoS_2@MoS_2@CC-30h	1 M KOH	87	87	20 h	Adv. Mater. Interfaces 2020, 7, 2000780
Cu@WC	1 M KOH	119	88.7	12 h	Appl. Catal. B-Environ. 2021, 280, 119451
Cu_3N-Cu_3P/NPSCNWs@NF	1 M KOH	68	69	24 h	ChemElectroChem 2020, 7, 289
$Cu_{0.075}Co_{0.925}P$/CP	1 M KOH	70	55.1	24 h	J. Mater. Chem. A, 2019, 7, 14271
FeP/NCNSs	1 M KOH	205	70	10 h	ACS Sustainable Chem. Eng. 2018, 6, 11587
FeP/Ti	1 M KOH	95	64	-	Appl. Catal. B-Environ. 2020， 260, 118156
$Fe_{0.43}Co_{2.57}(PO_4)_2$/Cu	1 M KOH	48.9	30.3	100 h	ACS Sustainable Chem. Eng. 2020, 8, 13793
CoP/CC	1 M KOH	209	129	22.5 h	J. Am. Chem. Soc. 2014, 136, 7587
CoP-CC	1 M KOH	95	60	72 h	ChemSusChem 2016, 9, 472
CoFeP/Ti	1 M KOH	78	75	20 h	Adv. Mater. 2017, 29, 1602441

CoFePO/NF	1 M KOH	87.5	38.1	100 h	ACS Nano 2016, 10, 8738
Co-P/NC	1 M KOH	150	51	24 h	Chem. Mater. 2015, 27, 7636
Co_2P/NF	1 M KOH	108	69	10 h	J. Mater. Chem. A 2017, 5, 16580
Co_2P@N,P-PCN/CNTs	1 M KOH	154	52	25 h	J. Mater. Chem. A 2016, 4, 15501
CoMoP@C/GC	1 M KOH	81	55.5	24 h	Energy Environ. Sci. 2017, 10, 788
rGO-few layer $FePS_3$	0.5 M KOH	192	-	1,000 CV cycles	ACS Energy Lett. 2016, 1, 367
Ni_3Se_2 nanoforest	1 M KOH	203	79	200 h	Nano Energy 2016, 24, 103
$CoSe_2$/CC	1 M KOH	190	85	12 h	Adv. Mater 2016, 28, 7527
$Ni_{0.33}Co_{0.67}S_2$	1 M KOH	88	118	20 h	Adv. Energy Mater. 2015, 5, 1402031
NiMoN film	1 M KOH	109	95	36 h	Adv. Energy Mater. 2016, 6, 1600221
P-Fe_3O_4/IF	1 M KOH	42	41.09	60 h	Adv. Mater. 2019, 31, 1905107

Co_6W_6C@NC/CC	1 M KOH	59	45.39	50 h	Small 2020, 16, 1907556
Mo-WC@NCS	1 M KOH	179	81	12 h	Nano Energy 2020, 74, 104850
CoP NW/Hb	1 M KOH	52	88	14 h	Nano Res. 2017, 10, 1010
$NiCo_2P_x$/CF	1 M KOH	58	34.3	30 h	Adv. Mater. 2017, 29, 1605502
Co-Ni-P film	1 M KOH	103	33	10 h	ACS Appl. Mater. Interfaces 2017, 9, 31887
Mo-Ni_2P/NF	1 M KOH	78	109	2,500 CV cycles	Nanoscale 2017, 9, 16674
$Mo_2F_xC_{1-x}$/rGO	1 M KOH	138	50	48 h	ACS Sustainable Chem. Eng. 2020, 8, 10284
Mo-Ni_2P/NF	1 M KOH	78	109	2,500 CV cycles	Nanoscale 2017, 9, 16674
MoP/CNT-700	1 M KOH	86	73	40 h	Adv. Funct. Mater. 2018, 28, 1706523

η_{10} is the overpotential at the current density of −10 mA cm^{-2} except those specified else.

All of the "-" means that no values were reported for the corresponding parameters in the corresponding references.

Table S5. Comparison of the HER performance of Rh-SA/$Ti_3C_2O_x$ with previously electrocatalysts in neutral conditions.

Catalysts	*Electrolyte*	η_{10} (mV vs RHE)	*Tafel* (mV dec^{-1})	*Stability*	*References*
Rh-SA/$Ti_3C_2O_x$	1 M PBS	85	77.4	24 h	This work
B-CoP/CNT	1 M PBS	79	80	100 h	Angew. Chem. Int. Ed. 2020, 59, 4154
Ce, N-CoP/CC	1 M PBS	72	56	60 h	Sustain. Energy Fuels, 2019, 3, 3344
CeO_2/Co_4N	1 M PBS	75	112	40 h	Appl. Catal. B-Environ. 2020, 277, 119282
Co@NG/NRGO	1 M PBS	400	89	40 h	Chem. Commun., 2020, 56, 567
$Co_{0.31}Mo_{1.69}C$/MXene/NC	0.1 M PBS	126	46	-	Adv. Energy Mater. 2019, 9, 1901333
Co-P@PC-750	1 M PBS	85	58	20 h	Small 2020, 16, 1900550
CoP-400	1 M PBS	161	81	70,000 s	Small 2018, 14, 1802824
CoP/Ni_2P@HPNCP	1 M PBS	141	85.92	20 h	Nanoscale, 2020, 12, 23851

Cu@WC	1 M PBS	173	118.3	12 h	Appl. Catal. B-Environ. 2021, 280, 119451
Cu_3N-Cu_3P/NPSCNWs@NF	1 M PBS	109	124.1	30 h	ChemElectroChem 2020, 7, 289
$Cu_{0.075}Co_{0.925}P$/CP	1 M PBS	120	97.5	24 h	J. Mater. Chem. A, 2019, 7, 14271
FeP/NCNSs	1 M PBS	409	92	10 h	ACS Sustainable Chem. Eng. 2018, 6, 11587
$Fe_{0.43}Co_{2.57}(PO_4)_2$/Cu	1 M PBS	53.8	91.5	100 h	ACS Sustainable Chem. Eng. 2020, 8, 13793
CoP/CC	1 M PBS	106	93	1,000 CV cycles	J. Am. Chem. Soc. 2014, 136, 7587
FeP/Ti	1 M PBS	102	-	16 h	ACS Nano 2014, 8, 11101
Fe-O-P NRs	1 M PBS	96	47	60 h	J. Mater. Chem. A 2018, 6, 9467
Mo-WC@NCS	1 M PBS	221	95	12 h	Nano Energy 2020, 74, 104850
CoP NW/Hb	1 M PBS	120	106	100 h	Nano Res. 2017, 10, 1010
Ni-C-N NSs	1 M PBS	92.1	38	70 h	J. Am. Chem. Soc. 2016, 138, 14546

SiO_2/PPy NTs-CFs	1 M PBS	187	100.2	30 h	Angew. Chem. Int. Ed. 2017, 56, 8120
$NiCo_2P_x$/CF	1 M PBS	63	63.3	30 h	Adv. Mater. 2017, 29, 1605502
Co-S/FTO	1 M PBS	160	93	40 h	J. Am. Chem. Soc. 2013, 135, 17699
$NiWS_x$/FTO	1 M PBS	373	96	-	Energy Environ. Sci. 2013, 6, 2452
CoW_x/FTO		271	78	-	
$CoMoS_x$/FTO		241	85	-	
$CoMoS_4$ NTA/CC	1 M PBS	104	77	32 h	Chem.-Eur. J. 2017, 23, 12718
$Mo_2F_xC_{1-x}$/rGO	1 M PBS	410	70	48 h	ACS Sustainable Chem. Eng. 2020, 8, 10284
Mo-Ni_2P/NF	1 M PBS	84	85	2,500 CV cycles	Nanoscale 2017, 9, 16674
MoP/CNT-700	1 M PBS	102	115	40 h	Adv. Funct. Mater. 2018, 28, 1706523

η_{10} is the overpotential at the current density of −10 mA cm^{-2} except those specified else.

All of the ”-” means that no values were reported for the corresponding parameters in the corresponding references.

Table S6. Comparison of HzOR performance in the alkaline media for Rh-SA/$Ti_3C_2O_x$ with other previously reported electrocatalysts.

Catalysts	Electrolyte	Potential (mV vs RHE)	References
Rh-SA/$Ti_3C_2O_x$	1.0 M KOH + 0.1 M N_2H_4	$E_{37.5}$ = 100	*This work*
		$E_{123.1}$ = 200	
		$E_{221.4}$ = 300	
Mn-SA/BNC	1.0 M KOH + 0.5 M N_2H_4	E_{10} = 132	Nanoscale 2021, DOI: 10.1039/D0NR09104A
PW-Co_3N NWA/NF	1.0 M KOH + 0.1 M N_2H_4	E_{10} = −55	Nat. Commun. 2020, 11, 1853
		E_{50} = −29	
		E_{200} = 27	
Co_3Ta/C	3.0 M KOH + 0.5 M N_2H_4	$E_{25.2}$ = 60	Nat. Commun. 2019, 10, 4514
Ni_xP/Ni foam	1.0 M KOH + 1 M N_2H_4	E_{172} = 100	Appl. Catal. B: Environ. 2019241, 292
Rh/N-CBs	1.0 M KOH + 0.05 M N_2H_4	E_{10} = 72	ACS Appl. Mater. Interfaces 2019, 11, 35039

Ni_3S_2/NF	1.0 M KOH + 0.2 M N_2H_4	E_{100} = 415	J. Mater. Chem. A 2018, 6, 19201
Ni_2P/Ni foam	1.0 M KOH + 0.5 M N_2H_4	E_{50} = −25	Angew. Chem. Int. Ed. 2017, 56, 842
Ni-NSA	3.0 M KOH + 1 M N_2H_4	$E_{227.6}$ = 250	Angew. Chem. Int. Ed. 2016, 55, 693
NiZn	1.0 M KOH + 1 M N_2H_4	E_{320} = 600	Angew. Chem. Int. Ed. 2014, 53, 10336
Ni_2P-HNTs/NF	1.0 M KOH + 0.5 M N_2H_4	E_{100} = 166	Nanoscale 2020, 12, 11526
Cu_1Ni_2-N	1.0 M KOH + 0.5 M N_2H_4	E_{100} = ~200	Adv. Energy Mater. 2019, 9, 1900390
S-CuNiCo LDH-3	1.0 M KOH + 0.02 M N_2H_4	E_{100} = ~700	J. Mater. Chem. A 2019, 7, 24437
Se/porous carbon membranes	1.0 M KOH + 0.1 M N_2H_4	E_{10} = ~450	Angew. Chem. Int. Ed. 2019, 58, 13466
Fe_2MoC@NC	1.0 M KOH + 0.1 M N_2H_4	E_{10} = ~500	Angew. Chem. Int. Ed. 2018, 57, 17168
$CoSe_2$/NF	1.0 M KOH + 0.5 M N_2H_4	E_{100} = −17	Angew. Chem. Int. Ed. 2018, 57, 7649
NiO_x-Pt/C	1.0 M KOH + 0.1 M N_2H_4	E_{100} = ~200	Appl. Catal. B-Environ. 2017, 201, 22
N-doped carbon	1.0 M KOH + 0.1 M N_2H_4	E_{10} = ~700	Angew. Chem. Int. Ed. 2017, 56, 13513

CoNi alloy@CoNi sulfide	1.0 M KOH + 2.0 M N_2H_4	E_{10} = ~150	Adv. Mater. 2017, 29, 1604080
Vertical graphene nano-hills-45	1.0 M KOH + 0.05 M N_2H_4	E_{10} = ~910	NPG Asia Mater. 2017, 9, e378.
FePc	0.2 M KOH + (-) N_2H_4	E_{100} = ~0.35	Talanta 2005, 67, 162
Cu nanoparticles	0.1 M KOH + 0.01 M N_2H_4	E_{100} = ~0.5	J. Mater. Chem. A 2014, 2, 4580
3D PNNF	3.0 M KOH + 0.5 M N_2H_4	E_{100} = ~0.125	Nano. Res. 2015, 8, 3365
FeN_4	0.2 M NaOH + (-)N_2H_4	E_{100} = ~0.4	Electrochem. Commun. 2013, 30, 34
$Ni_{0.6}Co_{0.4}$-ANSA	3.0 M KOH + 0.5 M N_2H_4	E_{100} = ~ –1 (V vs SCE)	Adv. Sci. 2017, 4, 1600179
Cu film	3.0 M KOH + 1.0 M N_2H_4	E_{100} = ~ –0.65 (V vs SCE)	Adv. Mater. 2015, 27, 2361
Fe-CoS_2 nanosheets	1.0 M KOH + 0.1 M N_2H_4	E_{100} = 0.129	Nat. Commun. 2018, 9, 4365

E_x is the potential at the current density of x mA cm^{-2} except those specified else.

Table S7. Comparison of H_2 production rate obtained on the Rh-SA/$Ti_3C_2O_x$ with other previously reported electrocatalysts.

Catalysts	*Electrolyte*	*H_2 production rate*	*References*
Rh-SA/$Ti_3C_2O_x$	1 M KOH + 0.1 M N_2H_4	45.77 mmol h^{-1}	This work
PW-Co_3N NWA/NF	1 M KOH + 0.5 M N_2H_4	1.25 mmol h^{-1}	Nat. Commun. 2020, 11, 1853
Fe-CoS_2	1 M KOH + 5.3 M N_2H_4	9.95 mmol h^{-1}	Nat. Commun. 2018, 9, 4365
PPy/FeTCPP/Co	1 M KOH	0.28 mmol h^{-1}	Adv. Funct. Mater. 2017, 27, 1606497
GO-PANi31-FP	0.1 M KOH	0.496 µL s^{-1}	Angew. Chem. Int. Ed. 2016, 55, 13296
$Fe_{0.5}Ni_{0.5}$@N-GR	1 M KOH	0.5 µL s^{-1}	Adv. Funct. Mater. 2018, 28, 1706928
WO_3/$BiVO_4$	0.5 M PBS + 1 M Na_2SO_3	7.27 µL min^{-1}	Nano-Micro Lett. 2020, 12, 88
Ti-Fe_2O_3	1 M NaOH	6.67 µL min^{-1}	ACS Nano 2018, 12, 8625